Advanced modeling of enhanced CO$_2$ dissolution trapping in saline aquifers
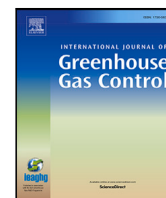
Lyu, Xiaocong; Voskov, Denis

Important note
To cite this publication, please use the final published version (if applicable).
Please check the document version above.

Advanced modeling of enhanced CO_2 dissolution trapping in saline aquifers

Xiaocong Lyu [a,b], Denis Voskov [b,c,*]

[a] *State Key Laboratory of Petroleum Resources and Prospecting, China University of Petroleum, Beijing, China*
[b] *Department of Geoscience and Engineering, TU Delft, Delft, Netherlands*
[c] *Department of Energy Resources Engineering, Stanford University, CA, USA*

ARTICLE INFO

ABSTRACT

A consistent thermodynamic model based on a combination of the Peng-Robinson equation of state for gas components with an activity model for the aqueous phase is utilized in this study to accurately evaluate the performance of geologic CO_2 storage in saline aquifers. To account for thermal effects, the phase enthalpy and conductivity are derived with consideration of CO_2 dissolution in brines. Several conceptual numerical setups with variations in parameters and physics are constructed to investigate the enhanced CO_2 dissolution in saline aquifers. In addition, a realistic geological structure is considered to evaluate the potential for storing CO_2 at the field scale. Our simulation results show that the presence of a capillary transition zone (CTZ) can significantly reduce the onset time and enhance the dissolution rate. The temperature has a crucial effect on the dissolution trapping compared to isothermal assumptions. Thermal conduction and convection suspend the onset of mass convection, while the final mass flux is augmented. Heat conduction smears out the temperature difference between rocks and fluids, thus suppressing thermal fingering. We demonstrate that the dissolution trapping in realistic 3D aquifers can be significantly different from their 2D analogues. The field-scale simulation results show that the dissolution rate increases sharply once the convection dominates the CO_2 migration which corresponds to a reduction of residual trapping. Besides, a high-resolution 3D model is required for accurately resolving the enhanced CO_2 dissolution in realistic heterogeneous reservoirs. An efficient multi-scale framework for an accurate evaluation of CO_2 trapping is proposed for this purpose.

1. Introduction

Geologic CO_2 storage (GCS) in deep subsurface formations is recognized as a promising technology for reducing greenhouse gas emissions from industrial activities (Anderson et al., 2005; Schrag, 2007). The large storage volumes of saline aquifers or other formations (e.g., depleted oil/gas reservoirs) are available for injecting CO_2 into these strata safely and economically (Gilfillan et al., 2009; Szulczewski et al., 2012). In the context of climate change, GCS projects have demonstrated its feasibility and are essential to lower CO_2 emissions.

In the carbon-sequestration in deep formations, supercritical CO_2 is injected into a saline aquifer and starts interacting with in-situ aqueous brine or rocks. Due to the density contrast, the lighter CO_2 migrates upwards and forms a CO_2-rich supercritical phase. A small amount of CO_2 dissolves into the underlying brine, resulting in density stratification (i.e., diffusive transport) (Ennis-King and Paterson, 2005; Jafari Raad et al., 2019). This small density increase of the brine induces gravitational instability. Afterwards, buoyancy-driven convection dominates the CO_2 migration with fingers of denser brine moving downward. This process can significantly enhance the dissolution rate, compared

with the rate dominated by purely diffusive transport (Lindeberg and Wessel-Berg, 1997; MacMinn et al., 2011).

The typical convective dissolution process in long-term CO_2 sequestration is governed by a combination of complex physical phenomena: diffusive and convective migration. Most detailed studies of this process usually only consider a single-phase system where an impermeable top boundary supplies a dense solute at constant concentration (Ennis-King and Paterson, 2005; Slim, 2014). In a realistic two-phase system, the capillary transition zone may increase the mass transfer. To investigate the physical nature of the interaction between buoyancy and viscous-related effects, Riaz and Tchelepi (2007) applied the stability analysis to a two-phase flow problem in homogeneous porous media and found that with a given capillary number, the numerical results closely match those obtained by the linear stability analysis. This model was further improved and validated against experimental results in Neufeld et al. (2010). Another attempt to connect simulation with experiments has been performed by Farajzadeh et al. (2009). Later, the analytical model was enhanced to account for capillary transition effects (Elenius

et al., 2014). Through numerical simulations of the two-phase problem with a capillary transition zone, many researchers have proved that two-phase convection can significantly reduce the onset time for convection and enhance CO_2 dissolution, compared with single-phase conditions (Elenius et al., 2015; Martinez and Hesse, 2016).

Pau et al. (2010) found that the model dimension is one critical factor influencing the convective dissolution and the dissolution rate in a three-dimensional (3D) model increases by 25% compared to the rate in 2D model. Meng and Jiang (2014) demonstrated that 3D effects could be significant in the convective dissolution while negligible in predicting the onset time. Similar conclusions were reached in Lyu et al. (2021b). This is because, in a 3D domain, fluid can move in all directions of the horizontal plane instead of moving along one horizontal line as in the case of 2D flow. In addition, the CO_2 dissolution flux strongly correlates with reservoir heterogeneity, especially with heterogeneous permeability (Taheri et al., 2012; Kong and Saar, 2013; Li et al., 2018). Because the dimensionless Rayleigh number, commonly employed to characterize instability (Slim et al., 2013), is highly dependent on permeability.

In all studies mentioned above, the Boussinesq approximation is usually utilized for evaluating the density change based on the variations of CO_2 concentration in the mobile and immobile zones, i.e., brine density linearly increases with the increase of CO_2 concentration. Phase viscosity is assumed to be constant either for single-phase or two-phase problems (Elenius et al., 2015; Martinez and Hesse, 2016). However, in real applications, all thermodynamic properties change with the variations of pressure, temperature and CO_2 concentration (Linstrom and Mallard, 2001; Mao and Duan, 2009; Islam and Carlson, 2012) which often significantly deviates from simplified assumptions. Class et al. (2009) investigated some problems related to CO_2 storage through a benchmark study where those fluid properties, such as phase density, viscosity and enthalpy, are calculated by different models. However, the effect of fluid properties on CO_2 dissolution was not appropriately addressed in their study. Very few studies focus on the CO_2 plume propagation and dissolution based on either a realistic thermodynamic model or large-scale 3D porous media due to the complexity and expensive computational cost.

In this work, we investigate the CO_2 dissolution with thermal effects based on a realistic thermodynamic model in both small-scale 2D and large-scale 3D porous media. To improve the computational efficiency, the Delft Advanced Research Terra Simulator (DARTS) is used to perform all simulations. DARTS has been proved to be an efficient and accurate simulator through a series of benchmark studies related to various energy applications (Khait and Voskov, 2018; Wang et al., 2020; Lyu et al., 2021a). In Lyu et al. (2021b), we have verified the capability of DARTS to model the complex physics during CO_2 dissolution process without thermal effect. Here, we extend our previous work by considering thermal effects in both small-scale 2D and large-scale 3D models. In addition, we proposed a multi-scale scheme to consider the enhanced CO_2 dissolution in large-scale reservoir simulation with realistic heterogeneity.

This paper is structured as follows. First, we briefly introduce our problem formulation followed by a description of the numerical framework and thermodynamic model. Next, we show our simulation capabilities for predicting the key features during CO_2 dissolution process in a 2D domain with thermal effects. Furthermore, the 2D studies are extended to large-scale 3D models to investigate the enhanced CO_2 dissolution. In addition, based on these results, we test the potential of CO_2 storage in a realistic heterogeneous aquifer. We conclude the paper by summarizing the main conclusions.

2. Problem formulation

2.1. Problem description

In this section, we describe three different scenarios with a brief problem-oriented motivation in detail (Fig. 1). Fig. 1(a) and (b) represent two cases in Scenario 1, that is, single-phase flow with the negligible effect of CTZ and two-phase flow with a realistic CTZ (the leading part of the CO_2 plume). The corresponding capillary number (C_a) with the CTZ is 10 to ensure that the instability problem is characterized by a transition regime ($1 < C_a < 10^4$) (Riaz and Tchelepi, 2007; Gasda et al., 2012). We assume that the dissolution of CO_2 does not impact the capillary pressure curve in the course of the simulation. These two models are the most used when one investigates CO_2 dissolution in aquifers. In this work, an efficient approach is used to solve similar problems. In Scenario 2, we focus on the thermal effects on the dynamic behavior of density-driven convection. In this Scenario, Case 2 (Fig. 1(b)) in Scenario 1 is further transformed into a 3D model to investigate the effect of model dimensions on CO_2 plume propagation behavior. It is worth to be noted that the selected Rayleigh–Darcy (R_a) number is in order of 10^3, which is relevant to typical brine aquifers. Following the results of the first two scenarios, we introduce a realistic geological structure following the West Pernis field with a heterogeneous aquifer reservoir (Fig. 1). We inject CO_2 by the well located at the bottom of the reservoir and investigate the propagation of CO_2 plume.

In Table 1, we summarize the properties used in simulations. In Scenario 1, all fluid properties are dependent on the thermodynamic state, but the temperature of the system is assumed to be constant (75 °C). In Scenarios 2 and 3, the thermal effect is taken into account by introducing a thermal gradient (2.5 °C/100 m) with and without an influence of thermal conduction. The variation of temperature can affect CO_2 solubility significantly (Duan and Sun, 2003), further enhancing the convective instability.

To accurately capture the dynamic behavior of CO_2 plume during the onset of convection, the dimensions of the simulation domain must be significantly larger than the dimensional critical wavelength λ_c, an indication of the length scales that have to be resolved by numerical simulations to capture the convective transport and the resulting solution trapping (Riaz et al., 2006). It is defined based on linear stability analysis,

$$\lambda_c = 96.23 \frac{\phi \mu \mathbf{D}}{K \Delta \rho g}. \tag{1}$$

Here, ϕ is porosity, K is absolute permeability, $\mathbf{D}$ is the diffusion coefficient, μ is the aqueous-phase viscosity, $\Delta \rho$ is the density difference between pure brine and CO_2-saturated brine, and g is the gravitational acceleration constant. With a variation of K, ϕ and $\mathbf{D}$ in the following investigated problems, the selected dimensions of the domain can ensure that the width of the domain is larger than λ_c. As shown in Elenius et al. (2015), the proposed mesh resolution (around meter scale, especially in a vertical direction) provides a numerically converged solution for enhanced dissolution phenomena. In Scenarios 1 and 2, a random uniform distribution between zero and 4.17×10^{-6} mol/mol is placed just below the CO_2 emplacement to trigger the instability between the interface. In Scenario 3, CO_2 is injected from the bottom side, after that the injection ceases to observe the CO_2 plume propagation and dissolution.

2.2. Conservation equations

The mathematical equations for the flow and transport of a two-phase multi-component thermal system in porous media are described by mass and energy conservation equations:

$$\frac{\partial}{\partial t}\left(\phi \sum_{j=1}^{n_p} x_{cj}\rho_j s_j\right) + div \sum_{j=1}^{n_p}(x_{cj}\rho_j \mathbf{u}_j + s_j \rho_j \mathbf{j}_{cj}) + \sum_{j=1}^{n_p} x_{cj}\rho_j \widetilde{q}_j = 0, \tag{2}$$

$$c = 1, 2 \cdots, n_c,$$

$$\frac{\partial}{\partial t}\left(\phi \sum_{j=1}^{n_p} \rho_j s_j U_j + (1-\phi)U_r\right)$$

$$+ div \sum_{j=1}^{n_p} h_j \rho_j \mathbf{u}_j + div(\kappa \nabla T) + \sum_{j=1}^{n_p} h_j \rho_j \widetilde{q}_j = 0, \tag{3}$$

(a) Single-phase flow
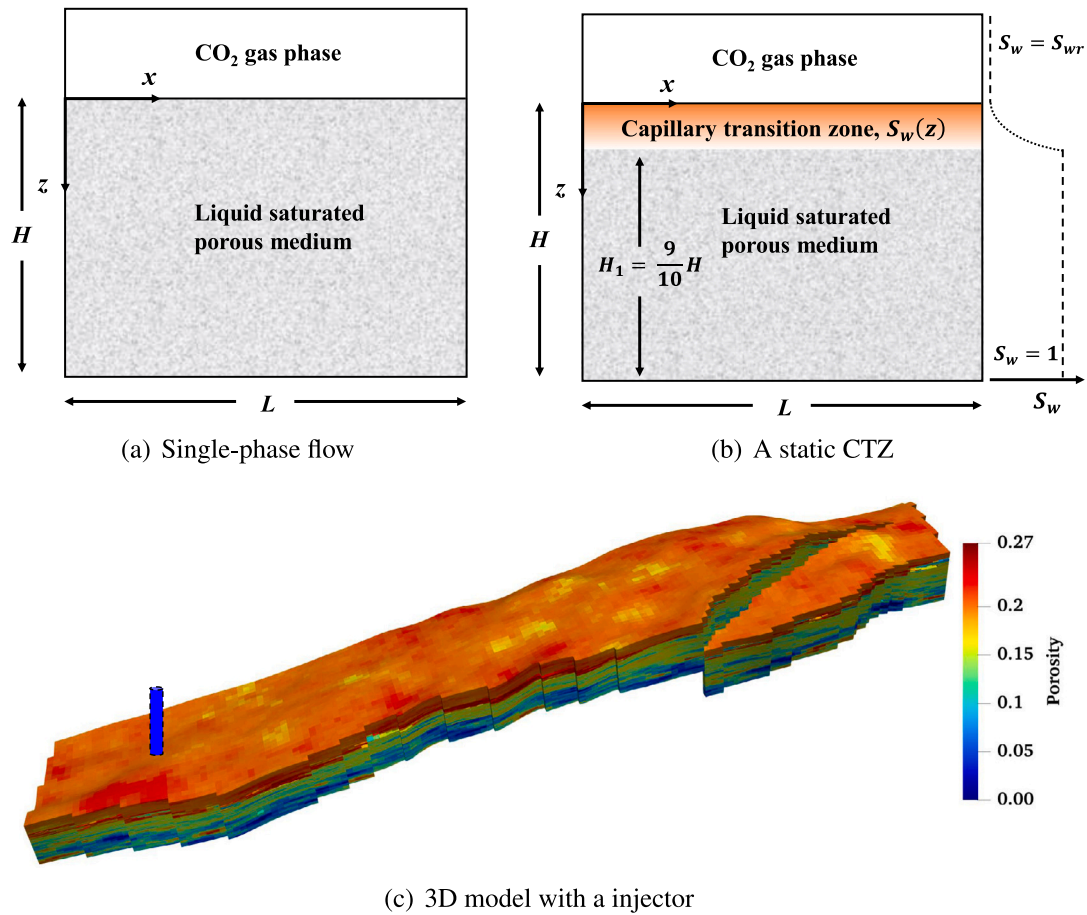
(b) A static CTZ

(c) 3D model with a injector

Fig. 1. Models used in this study. In (a), now-flow conditions are applied for all boundaries, and pressure is fixed at the top of the domain saturated with CO_2 by specifying a large pore volume; in (b), no-flow boundaries with a capillary transition zone present to provide CO_2, and the initial saturation and CO_2 concentration of the two-phase zone hold constant due to the large pore volume assumption; in (c), a large-scale 3D model with one CO_2 injector (blue bar).

Table 1
Summaries of properties used in each scenario.

	Parameters	Scenario 1		Scenario 2		Scenario 3
		Case 1	Case 2	Case1	Case 2	
Domain geometry	Depth, m	2475		2475		2610~3206
	Thickness, m	50		50		161.8~221.7
	Dimensions of model, -	100×50		100×50	$100 \times 100 \times 50$	$31 \times 150 \times 87$
	Gridblock size, m	0.5×0.5		0.5×0.5	$0.5 \times 1.0 \times 0.5$	–
Fluid properties	Phases	Single phase	Two phases	Two phases		Two phases
	CO_2 density, kg/m^3	f(state)		f(state)		f(state)
	Brine density, kg/m^3	f(state)		f(state)		f(state)
	CO_2 viscosity, mPa s	f(state)		f(state)		f(state)
	Brine viscosity, mPa s	f(state)		f(state)		f(state)
	CO_2 enthalpy, kJ/kmol	isothermal		f(state)		f(state)
	Brine enthalpy, kJ/kmol	isothermal		f(state)		f(state)
	Diffusion coefficient, m^2/s	2×10^{-9} (except where noted)				
Porous media properties	Permeability, mD	100 (except where noted)		100		0.24~1600
	Porosity	0.25 (except where noted)		0.25		1.4e^{-4}~0.27
	Residual brine saturation, S_{wc}	0.2				
	Residual CO_2 saturation, S_{gr}	0.2				
	Effective brine saturation, S_e	$S_e = (S_w - S_{wc})/(1 - S_{wc})$				
	Brine relative permeability	$k_{rw} = S_e^4$				
	CO_2 relative permeability	$k_{rg} = 0.4(1 - S_e^2)(1 - S_e)^2 - 0.0109$				
	Entry pressure p_e, bar	0.2				
	Capillary pressure, bar	$p_c = p_e/S_e^{0.5}$				
	Volumetric heat capacity, kJ/m^3/K	2200				
	Heat conductivity, kJ/m/day/K	180				

where subscript $j \in \{n, w\}$ denotes the nonwetting phase (supercritical CO_2) and the wetting phase (brine), $\mathbf{u}$ is Darcy velocity [m/day]. Besides, s_j, ρ_j, and x_{cj} are phase saturation, phase molar density [kmol/m^3], and component mole fraction in a phase, respectively. We defined $\mathbf{j}$ as Fick's diffusion flux [m^2/day], U_j and U_r are the fluid internal energy and rock internal energy [kJ], h_j is the fluid enthalpy [kJ/kg] and κ is the combined thermal conduction of rock and fluid [kJ/m/day/K].

In addition, Darcy's law is used to describe the advective flow of the multi-phase system with the presence of gravity and capillarity and Fick's law is used to describe the diffusive flux:

$$\mathbf{u}_j = -K \frac{k_{rj}}{\mu_j}(\nabla p_j - \rho_j g \nabla z), \tag{4}$$

$$p_w = p_n - p_c, \tag{5}$$

$$\sum_{j=1}^{n_p} s_j = 1, \tag{6}$$

$$\mathbf{j}_{cj} = -\phi D_{cj}\nabla x_{cj}, \tag{7}$$

where μ_j is the phase viscosity [mPa s] and k_{rj} is the phase relative permeability, p_j and z are phase pressure [bar], and the depth of the domain [m] and D_{cj} is the diffusion coefficient of component c in phase j. Capillary pressure p_c, often expressed as a function of saturation, is the pressure difference between the non-wetting p_n and wetting phase p_w, x is a mass fraction. Furthermore, the rock is compressible, reflecting the change of porosity with pressure through:

$$\phi = \phi_0(1 + c_r(p - p_{ref})), \tag{8}$$

where ϕ_0 is the reservoir initial porosity, p_{ref} is the reference pressure [bar] and c_r is the rock compressibility [bar^{-1}].

A finite-volume discretization on a general structured mesh based on a two-point flux approximation (TPFA) is implemented to discretize the domain in space. The backward Euler approximation is applied for the approximation in time to make the scheme fully implicit. The discretized mass conservation equations are expressed as (the energy conservation equation follows the same way):

$$V\left[(\phi \sum_{j=1}^{n_p} x_{cj}\rho_j s_j)^{n+1} - (\phi \sum_{j=1}^{n_p} x_{cj}\rho_j s_j)^n\right]$$
$$- \Delta t \sum_l \sum_{j=1}^{n_p} (x_{cj}^l \rho_j^l \Gamma_j^l \Delta \Phi^l + \phi \Gamma_d^l s_j^l \rho_j^l D_{cj}^l \Delta \chi_{cj}^l) + \Delta t \sum_{j=1}^{n_p} x_{cj}\rho_j q_j = 0, \tag{9}$$

where $\Gamma_j^l = \Gamma^l k_{rj}^l/\mu_j^l$ is a phase j transmissibility over interface l, and Γ^l is the constant geometrical part of transmissibility. Γ_d^l is the diffusive transmissibility. $\Delta \Phi^l$ and $\Delta \chi_{cj}^l$ are the pressure difference and component molar fraction difference at the interface l, respectively. After the linearization step, the Newton–Raphson method is adopted to solve the linearized system of equations on each nonlinear iteration in the following form:

$$J\left(\omega^k\right)\left(\omega^{k+1} - \omega^k\right) = -r\left(\omega^k\right), \tag{10}$$

where $J(\omega^k)$ and $r(\omega^k)$ are the Jacobian matrix and residual defined at the nonlinear iteration k, and ω is the primary unknown variables. In the conventional simulation, the Jacobian is assembled using accurate numerical property values and their derivatives with respect to nonlinear unknowns (variables used in nonlinear solutions). This process requires either various interpolations (for properties such as relative permeabilities of different phases) or a solution of a highly nonlinear system in combination with chain rule and inverse theorem (to address the sensitivity of the global Jacobian to flash results), see Voskov and Tchelepi (2012) for more details. In any case, the complexity of the simulation code and corresponding computational cost increase.

2.3. Operator-Based Linearization (OBL) approach

The Operator-Based Linearization (OBL) methodology has been proposed by Voskov (2017) following up the tie-simplex parametrization developed in Iranshahr et al. (2013a,b). With the OBL approach, the governing equations are written in the form of state-dependent operators by grouping all physical properties fully defined by thermodynamic state ω. This grouping transforms Eqs. (3) and (3) into the following form:

$$V\phi_0[\alpha_c(\omega) - \alpha_c(\omega_n)] - \Delta t \sum_l \sum_{j=1}^{n_p} (\Gamma^l \beta_{cj}^l(\omega)\Delta\Phi_j^l + \phi_0 \Gamma_d^l \gamma_{cj}^l(\omega)\Delta\chi_{cj}) = 0. \tag{11}$$

$$V\phi_0[\alpha_{ef}(\omega) - \alpha_{ef}(\omega_n)] - \Delta t \sum_l \sum_{j=1}^{n_p} [\Gamma^l \beta_{ej}^l(\omega)\Delta\Phi_j^l + \phi_0 \Gamma_d^l \gamma_j(\omega)\Delta\chi_{ej}]$$
$$+ (1 - \phi_0)VU_r[\alpha_{er}(\omega) - \alpha_{er}(\omega_n)] - \Delta t \sum_l (1 - \phi_0)\Gamma_d^l \kappa_r \alpha_{er}(\omega)\Delta\chi_{er} = 0, \tag{12}$$

where ω and ω_n are nonlinear unknowns in the current and previous timestep, respectively; $L(i)$ is the set of neighbors of the control volume l; $\Delta\Phi_j^l$ is the phase pressure difference between neighbor cells.

Here, the mass-conservation terms are defined as:

$$\alpha_c(\omega) = \left(1 + c_r(p - p_{ref})\right) \sum_{j=1}^{n_p} x_{cj}\rho_j s_j, \quad c = 1, \ldots, n_c; \tag{13}$$

$$\beta_{cj}(\omega) = x_{cj}\rho_j k_{rj}/\mu_j, \quad c = 1, \ldots, n_c, j = 1, \ldots, n_p; \tag{14}$$

$$\gamma_j(\omega) = \left(1 + c_r(p - p_{ref})\right)s_j, \quad j = 1, \ldots, n_p; \tag{15}$$

$$\chi_{cj}(\omega) = \rho_j D_{cj} x_{cj}, \quad c = 1, \ldots, n_c, j = 1, \ldots, n_p. \tag{16}$$

To keep a similar structure, the energy-related terms can be expressed as:

$$\alpha_{ef}(\omega) = \left(1 + c_r(p - p_{ref})\right) \sum_{j=1}^{n_p} \rho_j s_j U_j; \tag{17}$$

$$\beta_{ej}(\omega) = h_j \rho_j k_{rj}/\mu_j, \quad j = 1, \ldots, n_p; \tag{18}$$

$$\chi_{ej}(\omega) = \kappa_j T_j, \quad j = 1, \ldots, n_p. \tag{19}$$

In addition, to account for the energy and conduction of rock, two additional terms should be introduced:

$$\alpha_{er}(\omega) = \frac{1}{1 + c_r(p - p_{ref})}, \quad \chi_{er}(\omega) = T_r. \tag{20}$$

Here α_{er} and χ_{er} are used to represent the rock internal energy and rock conduction expressed in Eq. (3), respectively, T_r is the rock temperature [K], U_r is a state-dependent parameter, thus these two rock energy terms are treated separately.

Considering gravity and capillarity, the phase-potential-upwinding (PPU) strategy is selected to evaluate the numerical flux based on the phase-potential differences between the neighboring blocks (e.g., for phase j):

$$\Delta\Phi_{12} = p_1 - p_{c,1} - (p_2 - p_{c,2}) - \frac{\rho_j(\omega_1) + \rho_j(\omega_2)}{2}g(D_2 - D_1). \tag{21}$$

Here 1 and 2 are two neighboring blocks. The term Φ includes both state and space-dependent variables and needed to be split into linear and nonlinear parts for explicit evaluation of its values and derivatives. Thus, each phase should be treated separately, reflecting the increase of flux terms from n_c to $n_c n_p$ (Eq. (14)). Two terms should be added to reflect the effect of gravity and capillarity, expressed as:

$$\delta_j(\omega) = \rho_j g, \tag{22}$$

$$\zeta_j(\omega) = p_{c,j}, \tag{23}$$

where δ_j and ζ_j are gravity and capillarity terms, respectively, only dependent on the thermodynamic state. One can find more details about
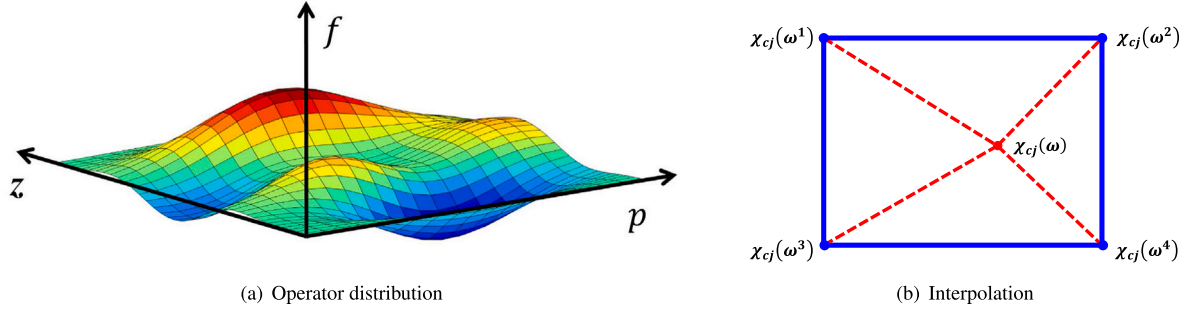
(a) Operator distribution

(b) Interpolation

Fig. 2. Schematic description of operator parametrization and interpolation process for χ operators with a predefined OBL resolution (modified from Voskov (2017) and Lyu et al. (2021a)). ω^1 to ω^4 are four supporting points, and ω is the current thermodynamic state of a given control volume at a given timestep in the simulation.

the applications of the OBL approach for multi-phase multi-component systems with gravity (Khait and Voskov, 2018), capillarity (Lyu et al., 2021a), thermal (Wang et al., 2020), and diffusion effects (Lyu et al., 2021b).

Conventionally, the evaluations of physical properties and corresponding derivatives with respect to nonlinear unknowns need to be performed in simulations, which is a complex and time-consuming process. However, the OBL approach provides a new strategy to decouple the computation of nonlinear physics, that is, parameterizing the state-dependent terms in physical space at the preprocessing stage or adaptively with a limited number of supporting points (Khait and Voskov, 2018). The parameter space depends on the investigated physical problem. In an isothermal CO_2-brine model, for instance, the nonlinear unknown variables are pressure p and CO_2 overal molar fraction z_{CO2}. If the OBL resolution is set as 100, a two-dimensional (2D) parameter space with $[100 \times 100]$ supporting points is constructed and the interpolation is executed in this 2D space. Then in the course of a simulation, the physical terms in the current timestep are evaluated based on a multi-linear interpolation strategy (Fig. 2), which improves the performance of linearization stage (Voskov, 2017). From Eqs. (13) to (19), there is no difference in format between mass- and energy-related terms except for those to describe the energy of rock (Eq. (20)). This treatment simplifies the Jacobian assembly using partial derivatives of physical terms with respect to nonlinear unknowns ω which are called operators and directly computed as coefficients in multi-linear interpolation.

2.4. Thermal properties for CO_2-brine system

In this work, the Peng-Robinson equation of state (PR-EOS) is employed to calculate the basic thermodynamic properties. With the assumption of local equilibrium, the multi-phase system should satisfy:

$$z_c - \sum_{j=1}^{n_p} v_j x_{cj} = 0, \tag{24}$$

$$f_c^g(p, T, \mathbf{x_g}) - f_c^w(p, T, \mathbf{x_w}) = 0, \tag{25}$$

$$\sum_{c=1}^{n_c} (x_{cg} - x_{cw}) = 0, \tag{26}$$

$$\sum_{j=1}^{n_p} v_j - 1 = 0. \tag{27}$$

Here $z_c = \sum_j x_{cj} \rho_j s_j / \sum_j \rho_j s_j$ is overall molar composition of component c and $f_{cj}(p, T, \mathbf{x_j})$ is the fugacity of component c in phase j. v_j is phase j molar fraction.

To accurately capture the phase behavior, a fugacity-activity model is employed to solve for thermodynamic equilibrium (Kritchevsky and Iliinskaya, 1945):

$$f_c^g = f_c^w \rightarrow p \psi_c y_c = h_c \kappa_c x_c, \tag{28}$$

where p is the total pressure, and ψ_c is the fugacity coefficient of the gas phase. h_c and κ_c are Henry's constant and activity coefficients. x_c and y_c are the molar fractions of each component in the aqueous phase and gas phase, respectively. Then we can obtain the K values for different gas components:

$$K_c = \frac{y_c}{x_c} = \frac{h_c \kappa_c}{p \psi_c}. \tag{29}$$

A standalone correlation proposed by Spycher et al. (2003) is used to reflect the equilibrium constant of the water component:

$$K_{H_2O} = \frac{y_{H_2O}}{x_{H_2O}} = \frac{K_{H_2O}^0}{\psi_{H_2O} p} exp(\frac{(p-1)V_{H_2O}}{RT}) \tag{30}$$

where $K_{H_2O}^0$ is the equilibrium constant of H_2O at the reference pressure of 1 bar, T is the temperature in Kelvins, V_{H_2O} is the molar volume of H_2O, and ψ_{H2O} is the fugacity coefficient of H_2O.

Considering the thermal problems of subsurface fluid, enthalpy is one important variable to describe the thermal effect, such as heat convection, heat conduction and heat generation. Based on the EOS model, enthalpy deviation is derived following the procedure suggested by Guo et al. (2019). In this model, enthalpy of the non-aqueous phase consists of two parts: the ideal enthalpy model of each constituent at a certain temperature and the enthalpy deviation model which indicates the enthalpy difference between an ideal gas and a real gas at the same pressure and temperature. In the aqueous-phase enthalpy model, the enthalpy-change term is added to take the chemical process of gas solubility into account. The validation of this EOS-derived enthalpy model vs. experimental results can be found in Guo et al. (2019).

3. Character of convective dissolution with isothermal assumptions

In this section, we study the main characteristics of convective dissolution in aqueous reservoirs at isothermal assumption.

3.1. Onset of convection

The presence of a capillary transition zone affects the onset of the natural convection because it allows vertical flow across the interface between the two-phase region and the diffusive boundary layer. Based on the linear stability analysis in a single-phase system (Ennis-King and Paterson, 2005; Riaz et al., 2006), the onset time is expressed by:

$$t_{onset} = c_0 \frac{\mu^2 \phi^2 D}{(\Delta \rho g K)^2}. \tag{31}$$

Fig. 3 demonstrates linear relations between t_{onset} and $1/K^2$, ϕ^2, and D in Eq. (31). We point out here that the onset time is defined based on the deviation of the simulated mass flux from a pure diffusive flux (Pruess and Zhang, 2008; Pau et al., 2010), i.e., the time at which the mass flux starts to increase. The onset time is sensitive to the
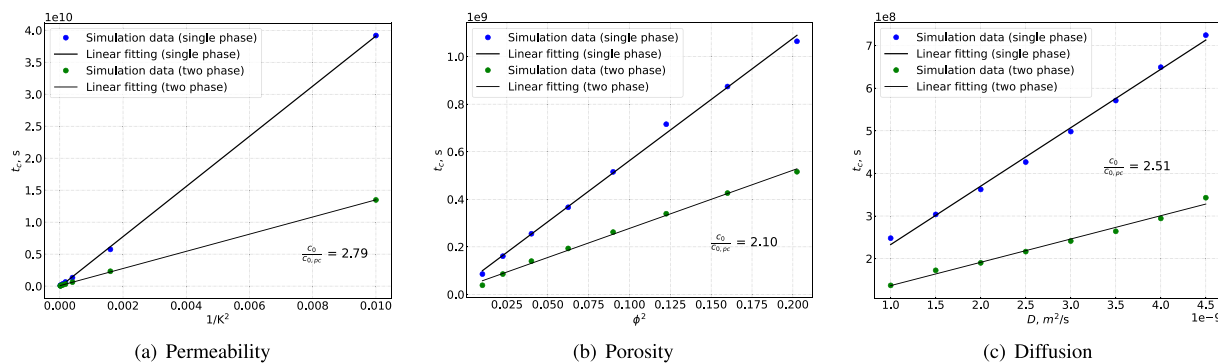
(a) Permeability   (b) Porosity   (c) Diffusion

Fig. 3. The relations between the onset of convection and permeability, porosity, and diffusivity. The dots denote the numerical data and the black solid lines represent the best linear fit. c_0 and $c_{0,pc}$ represent the constant expressed in Eq. (31), and the ratio between these two constants reflects the reduced onset time due to the presence of the capillarity transition zone. pc represents the case with consideration of the capillary-transition-zone effect.

perturbed variables investigated here and these perturbations incite convective instability in both cases. A l_2-fitting is performed based on simulation data to determine the gradient of the line for both cases with and without the capillary transition zone. In the case where the capillary transition zone is absent, we found c_0 to be 3066 (K), 3687 (ϕ), and 3147 (D), respectively; while in the case with the capillary transition zone, these values are 1127 (K), 1753 (ϕ), and 1255 (D). The variation of permeability holds the largest ratio of c_0, indicating that permeability affects the onset time more remarkably with consideration of the capillary transition zone. The magnitude of c_0 varies in a wide range in the literature (Ennis-King and Paterson, 2005; Ennis-King et al., 2005; Xu et al., 2006). The different criteria, which are used to define the onset time and the equation of states used in the simulations, are two important factors attributing to these discrepancies (Pau et al., 2010).

As mentioned above, the capillary transition zone plays a critical role in the onset of convection in a two-phase system (Riaz and Tchelepi, 2007). The presence of a capillary transition zone enhances the instability between the two-phase region and diffusive boundary layer. Fig. 3 shows that the onset time with a CTZ is shorter compared to that of the single-phase flow, decreasing by more than two-fold, smaller than the value (five-fold) in Elenius et al. (2012). The magnitude of reduced onset time depends mainly on the capillary number, which indicates the dominant regime in the instability problem. Meanwhile, the type of a capillary-pressure model can significantly influence the CO_2 solubility trapping (Li et al., 2013).

3.2. Long-term enhanced dissolution rate

Convection mainly dominates the mass transfer after the nonlinear onset time. The heavier CO_2-rich brine migrates downward in separate fingers while the upwelling currents of fresh brine penetrate into the two-phase region. This process substantially augments the dissolution rate, compared to a purely diffusive process. Pruess and Zhang (2008) found that the CO_2 mass flux stabilizes to a mean value and fluctuates with a $\pm15\%$ deviation from the mean. This point has been proven in Elenius et al. (2015) where authors derived two semi-analytical equations which can be used to explicitly and roughly predict the constant mass flux with the presence of the CTZ:

$$F = (-0.011 log(d) + 0.016)\frac{K\Delta\rho_w g X_{max}\rho_w(X_{max})}{\mu_w},\tag{32}$$

and at the negligible effect of the CTZ:

$$F = 0.021\frac{K\Delta\rho_w g X_{max}\rho_w(X_{max})}{\mu_w},\tag{33}$$

where X_{max} is CO_2 maximum mass fraction in brine [kg/kg], and d is the exponent of the relative-permeability function which is obtained by fitting the water relative permeability. In our study, d is a constant

with a value of 0.0516. All details about these parameters can be found in Elenius et al. (2015).

Fig. 4 presents the mass flux of dissolved CO_2 in brine, respectively. The dynamics of the dissolution–convection process in both cases show similar behavior: (1) initially the dissolution occurs by diffusion and it decays with time, proportionally to $t^{-1/2}$; (2) eventually, CO_2-rich brine amplifies the instability along the diffusive boundary and the layer becomes gravitationally unstable, leading to a flux-growth regime; (3) once fingers are sufficiently long and start to interact with their neighbors into a larger finger, the constant-flux regime occurs; (4) finally, fingers arrive at the bottom boundary and the overall concentration of the entire layer increases in a shut-down regime where the mass flux decreases with time.

The dissolution rate, CO_2 mass transferring to the single-phase brine region across the interface, is defined as $F = h\phi\frac{\partial\bar{c}}{\partial t}$ (h and $\bar{c}$ refer to the thickness and mean concentration of the single-phase brine region). The presence of the capillary transition zone has a negligible effect on the diffusive regime; however, it reduces the onset time significantly (Fig. 4). Once the convection dominates the mass transfer, the dissolution rate increases and eventually stabilizes close to a constant value. The constant value increases by around 2.5 times when a realistic two-phase region is taken into account. In addition, our simulation results have good agreement with solutions predicted by Eqs. (32) and (33), though there are some deviations from the constant value. In the shut-down regime, the capillary transition zone causes the dissolution rate to decrease faster due to the limited volume and a higher concentration. In Slim (2014), authors found that the dissolution rate is proportional to $1/(t+g)^2$ in single-phase convective mixing. By fitting the data in the shut-down regime, the coefficient $g \approx -1000$ shows a good match, but it cannot predict the decreasing mass flux with a capillary transition zone accurately.

Fig. 5 shows a sequence of snapshots of the profile of CO_2 molar-mass fraction in the aqueous phase. During the convection-dominated flow, these fingers grow up and move downward due to the higher density. The lighter fluid expands horizontally and pushes nascent fingers into one another once it migrates to the top boundary. This process finally makes adjacent small fingers merge together into some extended fingers with higher downward velocity. Once the leading tip of these fingers reaches the bottom boundary, it spreads horizontally and fills up the domain gradually. Fig. 5(b) explicitly shows that the presence of a capillary transition zone obviously enhances CO_2 dissolution corresponding to a shorter onset time and a higher concentration in aquifers at the same time, compared to the single-phase convective mixing. While similar conclusions have been reported before (Riaz and Tchelepi, 2007; Elenius et al., 2014), in this numerical study we utilize a newly proposed operator-based linearization approach which allows us to significantly improve the performance of the simulation. Systematic validation of our numerical approach to accurately represent
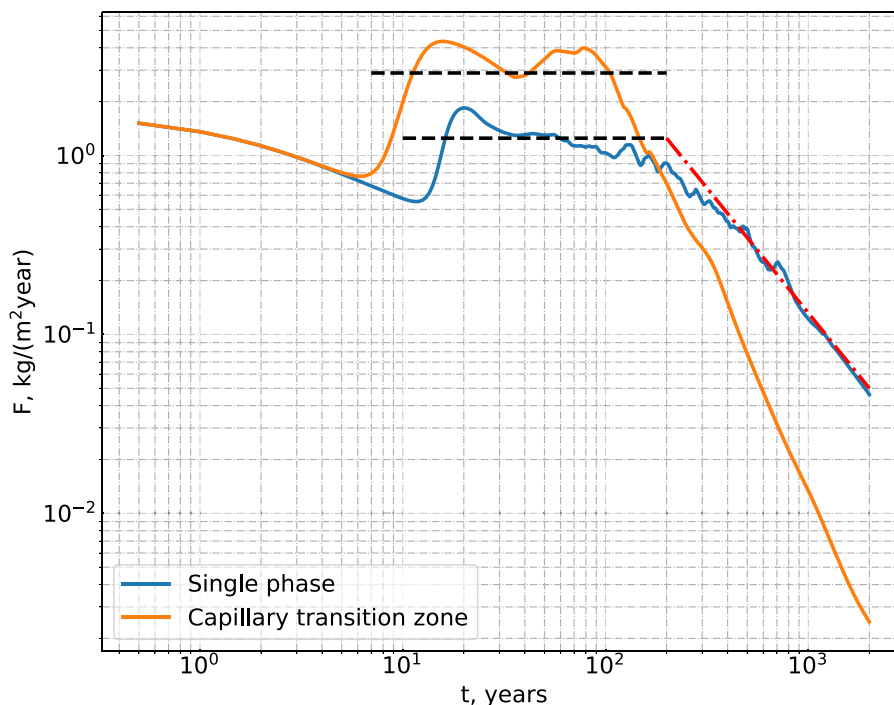
Fig. 4. Variations of CO_2 mass flux into the single-phase brine with time. Two black dashed lines are constant flux predicted by Eqs. (32) and (33). The red dashed line is the linear fitting in the shut-down regime. In this study, all fluid properties are dependent on the thermodynamic state, thus average properties are used to evaluate the constant mass flux.

this physical phenomenon at a large range of parameters confirms OBL employment for efficient and accurate simulation of CO_2 sequestration applications.

4. Thermal effect on convective dissolution with capillary transition zone

Once the denser fluid is transported convectively from the high-concentration region, heat is also transported through convective and conductive fluxes. In a short time, heat convection may dominate this process, but in long run, heat conduction also plays an important role because it can heat up cold CO_2 plumes. Thus in this work, we investigate the effect of heat convection and heat conduction separately.

Fig. 6 illustrates the impact of thermal effect with and without considering thermal conduction on the convective dissolution of CO_2 into brine at 50 years. Based on the CO_2 mole fraction in the aqueous phase, the lateral propagation of fingers in the isothermal case seems slower, corresponding to a thinner finger (less merging). The shape of CO_2 fingers is different in cases where thermal conduction is considered and excluded (Fig. 6(b) and (c)). Note that we remove the effect of heat conduction by setting the conductivity of both brine and rock to 0. Besides, thermal conduction between rocks and fluids smears out the temperature difference, that is, a smooth temperature gradient, as shown in Fig. 7(b). If heat conduction is neglected, heat transfer is only dominated by the convective flow. Therefore, heat fingers are generated along with mass fingers (Fig. 7(a)).

Table 2 shows the onset time and constant mass flux in the three cases mentioned above. The initiation of convective flow is suspended in cases with thermal effects, mainly due to the different directions of thermal gradient and concentration gradient along with the interface. The onset time is postponed by around $8 \sim 20\%$ with thermal effect. Again, heat conduction alleviates temperature difference between neighbors, leading to a relatively shorter onset time, compared to that without heat conduction. The mass flux in the constant regime is also distinct, though the differences are not momentous. By considering the heat transfer, the constant mass flux increases by 9.5% (with

Table 2
Comparison of onset time and constant mass flux in three different sets.

Parameters	Isothermal	Non-Iso A	Non-Iso B
Onset time, days	2432	2632	3053
Mass flux, kg/(m^3 year)	1.58	1.73	2.02

Note: Non-Iso A and Non-Iso B represent a non-isothermal process with conduction and without conduction, respectively.

conduction) and 27.8% (without conduction). In reality, when CO_2 is injected into aquifers, heat conduction and convection always coexist due to the natural geothermal gradient and mass convection. Therefore, the maximum mass flux increases by a limited number, but it could be a considerable amount of mass which may be underestimated without involving thermal effects in field-scale simulations.

Fig. 8 illustrates the variations of mass flux with time under different temperature gradients. In order to reduce the computational cost, we adopt a relatively higher temperature gradient than the typical geothermal gradient. These temperature gradients can be regarded as a vertical extension of the investigated domain. Fig. 8(a) shows that heat convection does not affect the diffusive process, reflecting the overlapping lines with different temperature gradients. The onset time varies in a relatively small range. Furthermore, the pronounced constant mass-flux regime disappears due to heat convection. Instead, the mass flux continuously increases until the CO_2 plume reaches the bottom boundary when the dissolution ability is restricted. With a higher thermal gradient, the mass-transfer rate with the constant regime also is enhanced. However, heat conduction agitates the mass diffusive process, corresponding to a relatively greater diffusive mass flux (Fig. 8(b)). The diffusive mass flux increases with the increasing temperature gradient. In addition, due to heat conduction, the onset time under different temperature gradients is nearly identical and the flux in the constant regime approaches each other.
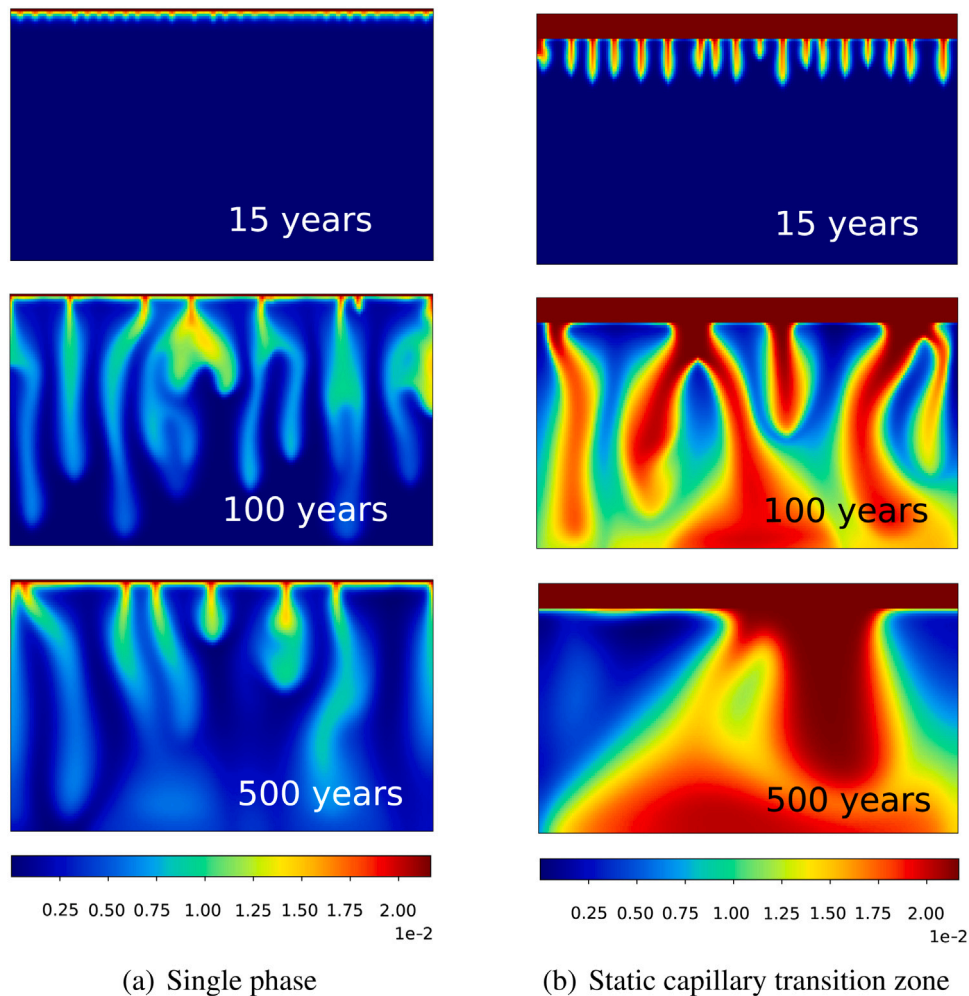
(a) Single phase

(b) Static capillary transition zone

Fig. 5. Propagation of CO_2 fingers with time.
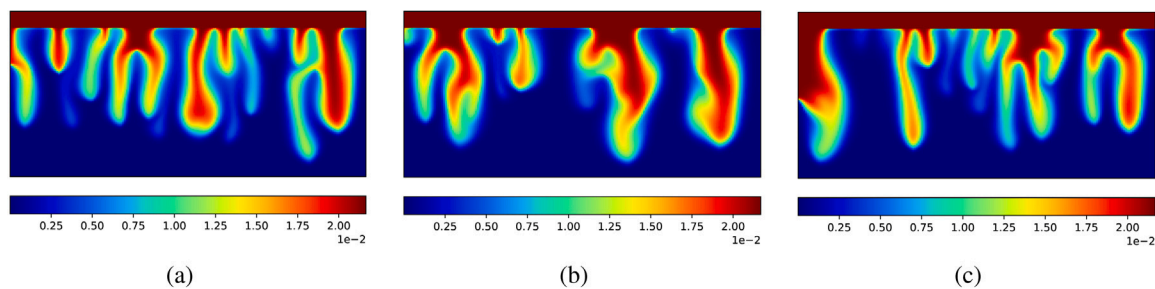

(a)

(b)

(c)

Fig. 6. CO_2 mole fraction profile at 50 years. (a) isothermal process; (b) non-isothermal with no conduction; (c) non-isothermal with conduction.

5. Influence of model dimensions

A 3D simulation of the diffusion–convection process is performed to investigate whether the model dimension significantly affects the results in comparison to a 2D simulation. Since a 3D simulation is computationally expensive due to a large number of degrees of freedom, we only examine one set of hydro-geologic parameters, see Table 1.

Figs. 9 and 10 show the evolution and structure of the 3D CO_2 fingers. At early time, the heels of fingers are connected with each other (Fig. 9(a)), while the 3D tips are approximately cylindrical in shape

(Fig. 9(b)), as seen in 2D simulations (Fig. 5(b)). The internal pattern of CO_2 fingers is also similar to 2D simulation. However, when pockets of lighter fluid (moving upward) reach the top boundary, they move outward in all directions of the horizontal plane instead of moving along one horizontal line as in the case of 2D flow. Therefore, some heels merge and become larger (Fig. 10(a)). As time progresses, the fingers grow larger and flatter. Due to the interaction among fingers, the 3D fingertips show a less rounded profile compared to those in 2D simulations (Fig. 10(c) and (d)). These observations demonstrate the qualitative differences between the 2D and 3D CO_2 fingers.
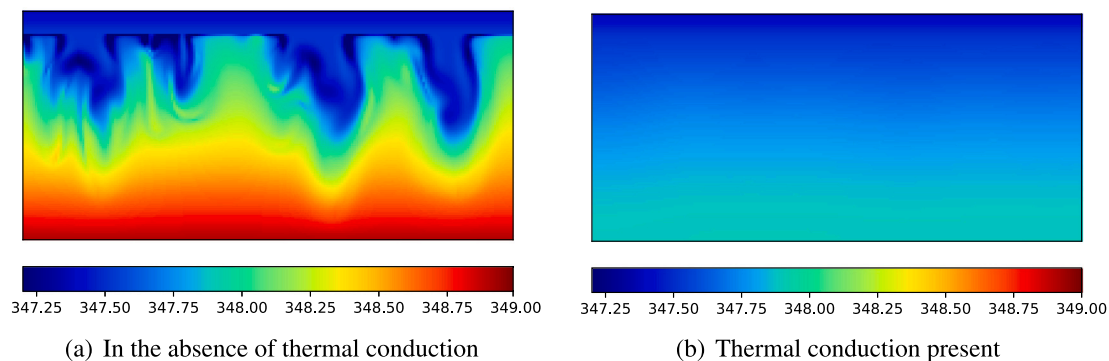
(a) In the absence of thermal conduction

(b) Thermal conduction present

Fig. 7. Temperature profile at 50 years.

(a) No conduction

(b) Conduction
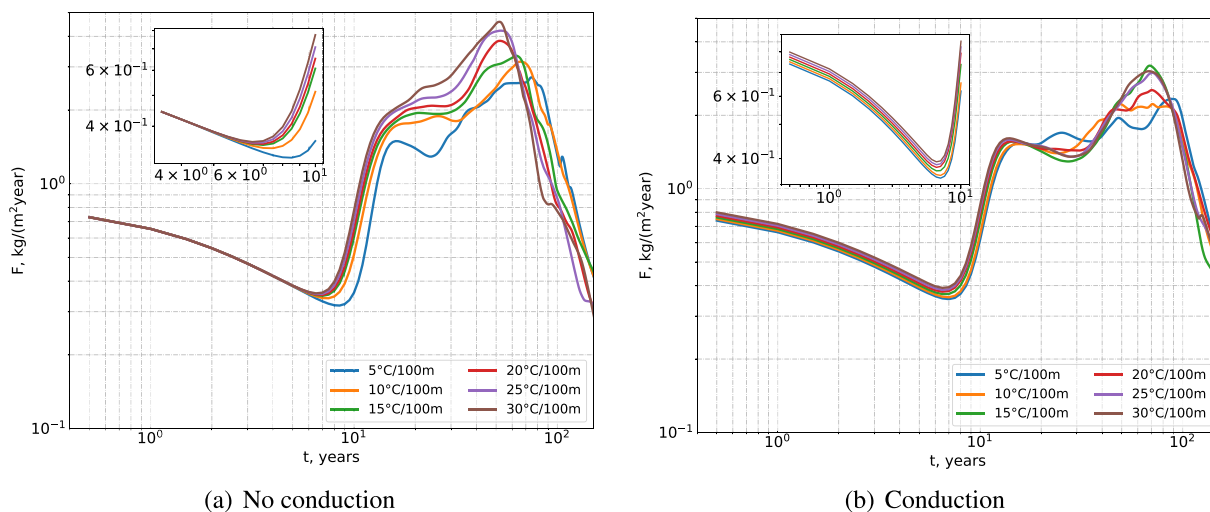
Fig. 8. Variations of CO_2 mass flux into single-phase region under different temperature gradient.

(a) Top
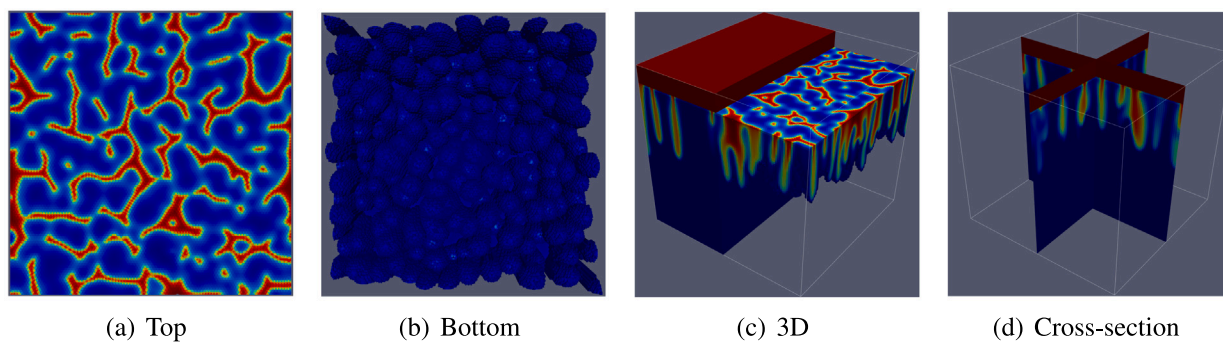

(b) Bottom

(c) 3D

(d) Cross-section

Fig. 9. Evolution of CO_2 fingers in the presence of a CTZ at 50 years. In (a), the CTZ zone saturated with CO_2 is removed for a better view; similarly, in (c), a threshold ([0.001, 0.0225]) is applied to illustrate the migration of CO_2 fingers inside the model.

Table 3 shows the comparison of the onset time and constant dissolution rate among 2D and 3D cases with and without the influence of thermal conduction. The onset time of 3D models is relatively shorter than that of 2D models due to the additional degrees of freedom. The increased degrees of freedom add significant complexity to the fingering phenomena. The mass flux also increases in the 3D model by approximately 23% compared to that of the 2D configuration with

consideration of thermal conduction. However, if thermal conduction is neglected, the increment of the mass flux in the 3D model is around 19%. In both models, the mass flux is reduced when thermal conduction is involved in the simulation. It is because heat conduction can recharge the CO_2 plumes, causing a comparatively lower dissolution capability. These results indicate that in a real CO_2 project, the amount of CO_2
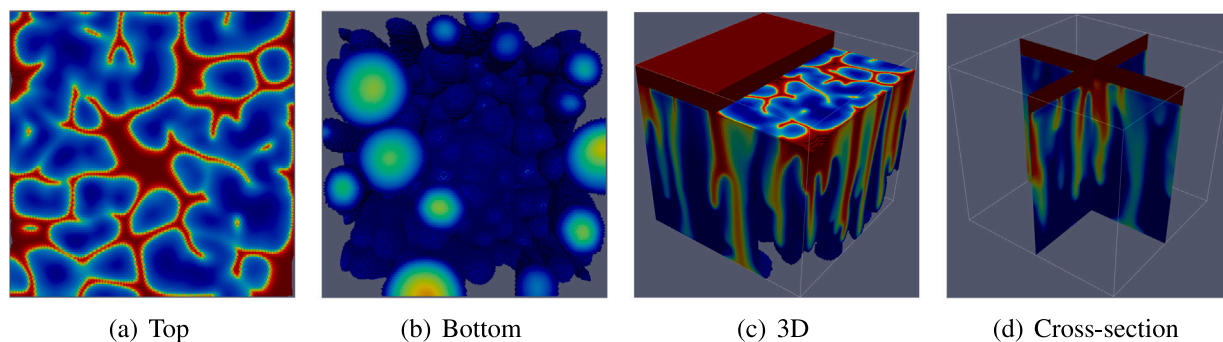
(a) Top   (b) Bottom   (c) 3D   (d) Cross-section

Fig. 10. Evolution of CO_2 fingers in the presence of a CTZ at 100 years. In (a), the CTZ zone saturated with CO_2 is removed for a better view; similarly, in (c), a threshold ([0.001, 0.0225]) is applied to illustrate the migration of CO_2 fingers inside the model.

Table 3
Comparison of onset time and constant mass flux between 2D and 3D models.

Parameters	2D conduction	2D excluding conduction	3D conduction	3D excluding conduction
Onset time, years	7.64	8.90	7.25	8.65
Constant rate, kg/(m³ year)	1.78	2.08	2.12	2.56

stored could be larger than that expected based on the 2D-simulation evaluation.

6. Case study based on West Pernis geology

In this section, we apply the developed modeling methodology to a large-scale model of the aqueous reservoir with detailed geology typical for North Sea. Besides, we propose a multi-scale methodology allowing us to accurately account for enhanced dissolution at the reservoir scale.

6.1. Field-scale simulations

Here, we present a real geological structure based on the West Pernis reservoir in the Netherlands with enhanced permeability typical for aquifers. We assume that the reservoir is fully saturated with water and all boundaries are closed. The reservoir average pressure and temperature are 79 bar and 92 °C, respectively. The CO_2 injection rate is 600×10^3 kg/day with a lower temperature of 40 °C and with a maximum bottom-hole-pressure (BHP) constraint of 300 bar, above which the formation may be damaged. After two years of injection, the well was stopped and the migration of CO_2 plume is monitored.

Fig. 11 shows the distribution of pressure, temperature, and gas saturation after injection. The reservoir pressure increases with injecting CO_2, approaching the fracturing pressure gradually. In the two-year injection period, the maximum reservoir pressure is still below 300 bar. The injected cold supercritical CO_2 spreads in the formation. However, due to the recharge of heat conduction, the leading edge of temperature, which only surrounds the injector, is far away from that saturation. The cold CO_2 plume is heated by the in-situ fluids and rocks under thermal convection and conduction, thus the temperature difference is smeared out. It also indicates that the supercritical CO_2 injection to extract energy is one efficient alternative for carrying out a geothermal project (Ezekiel et al., 2020).

Once the injection ceases, the supercritical CO_2 plume starts to migrate upwards in the formation and dissolve into the underlying brine gradually (Fig. 12). In this case, CO_2 plume arrives at the faults in 100 years. However, there is no connection between the upper wall and footwall, thus CO_2 cannot leak along the faults (i.e., safe fault). Fig. 12(a) shows that pressure decreases with the dissolution of CO_2, which reduces the risk of cracking overburden rock. The gas saturation is highly nonuniform mainly due to the heterogeneity of the formation. After ceasing injection, CO_2 plume propagates along the high-permeability channels under the gravity force, increasing the

contact area of CO_2 with brine and thus enhancing the chance of dissolution for permanent trapping. As shown in Fig. 12(b), the free gas exists mainly in residual conditions after 100 years. There are some spots where CO_2 already completely dissolves into the brine. In the process of CO_2 spread, the cold plume is heated, leading to an invisible temperature difference between the resident brine and CO_2 plume (Fig. 12(c)).

Fig. 13 demonstrates the variations of CO_2 mass in different conditions with time after ceasing injection. With the migration of CO_2 plume, the contact area of CO_2 with the underlying brine increases, causing an increasing amount of residual gas. Meanwhile, the increment of the contact area enlarges the dissolution trapping. However, once the free gas cannot spread in the field, i.e., the contact area is limited, the amount of residual gas starts to decrease due to gas dissolving into the brine. The dissolution gradually plays a dominant role in the trapping. Based on the idealized relationship proposed in Elenius et al. (2014), the total contact area can be expressed as $A(t) = 2t/3 \times 10^6$ m², where t is time after the start of injection, in years. The dissolution flux is estimated at 18.54 kg/(m² year), which is close to the value in the Utsira formation in the North Sea (17.73 kg/m²/year), see Elenius et al. (2014) for details. Notice that the effect of dissolution in large-scale simulation is underestimated since the resolution of the grid is too coarse to model enhanced dissolution correctly. Next, we are going to describe how this problem can be mitigated without introducing an excessive number of grid blocks to the full field model.

6.2. Multi-scale modeling of enhanced dissolution

To accurately capture the detailed enhanced dissolution phenomena, a fine mesh is required, which is computationally expensive. In this work, a multi-scale modeling technique is adopted to represent the enhanced dissolution process. Two representative elements are chosen: one is close to the injection well where the capillary transition zone is present; another element is in the region where the capillary effect can be neglected. Both elements are nine-block columns preserving the same geological properties as the original model. We mainly focus on the CO_2 migration in the central column, but the surrounding eight blocks are used to reflect the areal plume interaction. Here, we only run simulations using these two elements because they represent the CO_2 migration in the post-injection process. This process can be repeated for each reservoir column to account for dissolution trapping in the entire reservoir domain.

The two elements are refined into 120×120 mesh in the x-y plane (each block is 40×40), while the size in the *z*-direction keeps
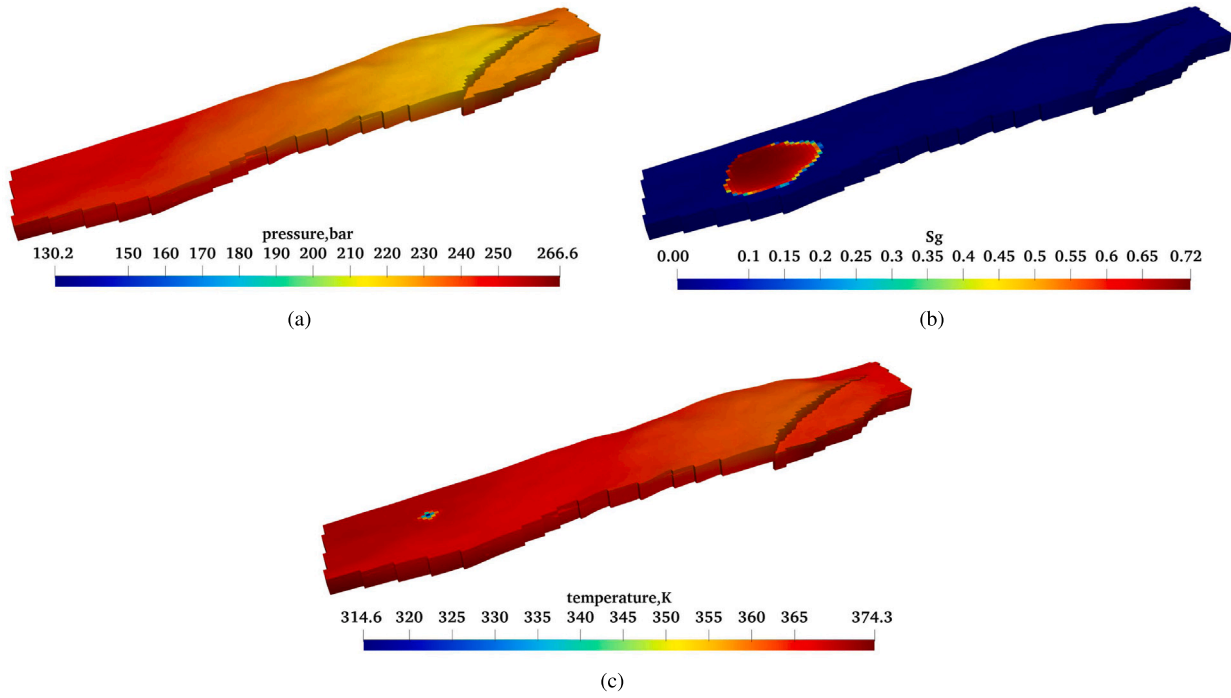
Fig. 11. Distribution of pressure, gas saturation and temperature after CO_2 injection.
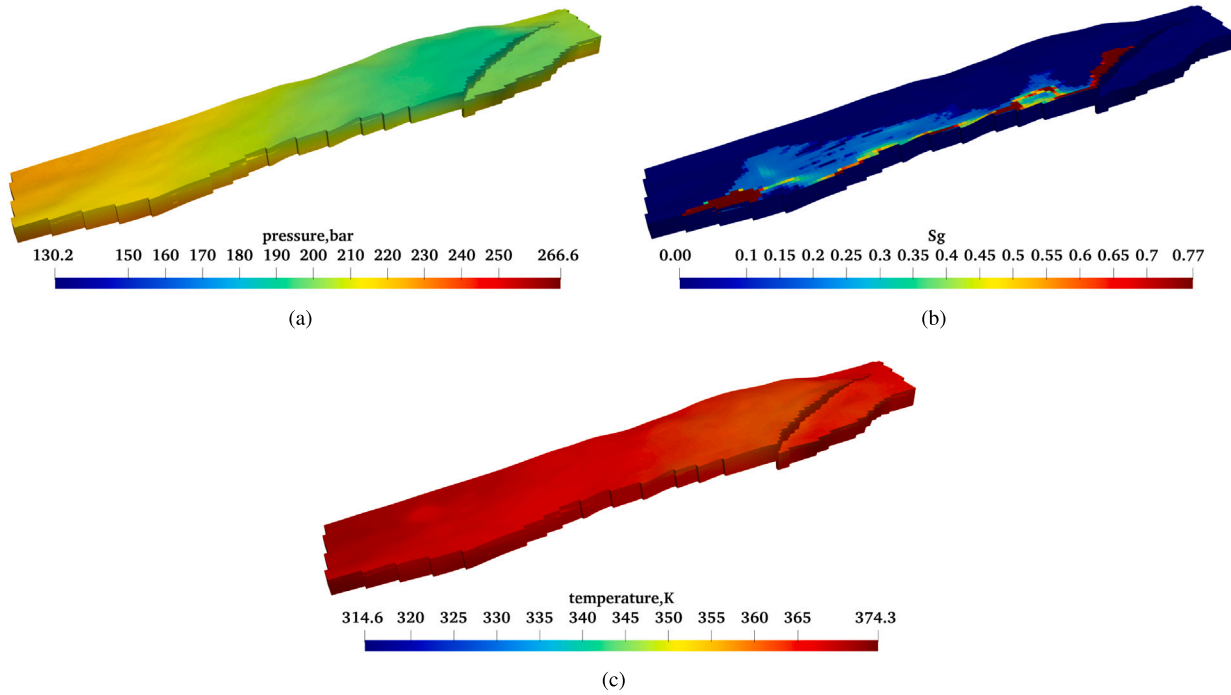

Fig. 12. Distribution of pressure, gas saturation and temperature in 100 years after CO_2 injection.
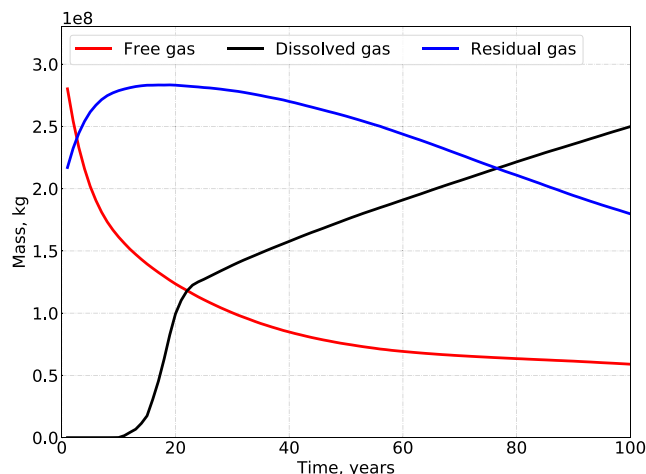
Fig. 13. Variations of CO_2 mass in different conditions after CO_2 injection.

the same with corresponding heterogeneity (Fig. 14). With this finer mesh (resolving to the meter scale), the numerically converged solution for enhanced dissolution phenomena can be pledged with an accurate representation of heterogeneity. The initial state of the elements is also identical to the average state of those columns in the field-scale model.

Fig. 15 shows CO_2 concentration after 100 years in both elements. After the onset of convection, CO_2 gradually dissolves into the underlying brine. With the consideration of the capillary effect in Element 1, CO_2 moves faster with a relatively higher concentration, which is consistent with the conclusion in Section 3.2. Due to the vertical heterogeneity, CO_2 fingers are not significantly scattered especially when CO_2 fingers reach the lower-permeability layers. It starts to propagate laterally and fills in the domain progressively. The increase of average CO_2 concentration reduces the dissolution rate. Without the capillary transition zone in Element 2, the fingers are relatively thinner and move slower mainly due to the low permeability.

Fig. 16 compares the mass transfer rate in different elements. In Element 1 (closer to the injection well), the mass transfer rate decreases firstly (diffusion-dominate regime) and reaches a fairly constant value of approximately 18.95×10^3 kg/year, corresponding to the convection-dominant regime. After 150 years, it decays gradually due to the interaction between CO_2 fingers and the low-permeability layer. Similar behavior can be observed in Element 2, the mass transfer rate is stabilized around 10.48×10^3 kg/year after the diffusion regime and it starts to decrease only after approximately 200 years due to the slower propagation velocity. However, the ratio of constant flux between Element 1 and 2 is around 1.8. This is different from the comparison performed in Section 3 where the difference in the dissolution rate between the single-phase and two-phase models is close to 2.5. This is because the distribution of vertical permeability of Element 1 and 2 are different and the reservoir heterogeneity plays an important role in the enhanced dissolution. The average mass transfer rate in the original model, which is the product of the average total mass in a unit area and the area of a one-block column, is around 25.95×10^3 kg/year, which is much higher than that of both Element 1 and 2.

Because the vertical heterogeneity in the realistic column model limits the vertical propagation of CO_2, and it further reduces the dissolution rate. Notice that such an effect of reservoir heterogeneity cannot be taken into account in the evaluation of the average mass transfer rate using analytic methods.

At the same time, in the coarse (field-scale) resolution, the dissolution is mostly driven by diffusion since the modeling resolution is not sufficient to account for the fingering. Thus, the dissolution rate decreases sharply with CO_2 propagation (Fig. 16). This investigation indicates that CO_2 sequestration simulation in realistic reservoirs can either overestimate (using the semi-analytic technique) or underestimate (using direct numerical simulation) the enhanced dissolution rate. A high-resolution simulation is required for accurately predicting the enhanced dissolution rate in the presence of realistic heterogeneity and proper variation of thermodynamic parameters. However, the computational cost of doing full-field simulations at appropriate resolution is very high. This study suggests an application of a multi-scale approach where enhanced dissolution can be corrected based on a localized high-resolution simulation.

7. Discussion

Density-driven convection enhances CO_2 dissolution in saline aquifers. This process strongly depends on geological and fluid parameters which reflect the value of the Rayleigh number. In practice, the formation is usually heterogeneous. Besides, the interaction between CO_2 and in-situ brine is quite complicated. These effects should be taken into consideration in the process of the Rayleigh-number evaluation.

Temperature is one critical parameter affecting the onset of convection and long-term enhanced dissolution. In large-scale simulations where the temperature varies significantly, the dissolution rate evaluated based on isothermal correlations may be not reliable due to the deviation of fluid properties (Someva et al., 2000). While in small-scale simulations, the dissolution rate exhibits a negligible dependence on the temperature.

In this study, we do not consider the effect of impurities on the dissolution rate in the depleted gas reservoir. This assumption is not rigorously correct because the residual gas saturation is not zero even in an abandoned gas reservoir. In addition, we select several blocks and refine them in multi-scale modeling to obtain a relatively accurate evaluation of CO_2 dissolution in aquifers. However, this representation may not capture the interactions between neighboring and targeted blocks. In terms of density-driven convection, the lateral propagation is not very strong. This treatment can be regarded as one efficient option for large-scale CO_2 storage simulations.

8. Conclusions

In this work, we investigate the propagation of CO_2 plume in saline aquifers by considering the realistic variation in thermodynamic parameters. The complex phase behavior of the CO_2-brine system is expressed by a fugacity-activity model, combined with phase enthalpy and conductivity involving CO_2 dissolution in aquifers. The highly nonlinear numerical problems are solved using the Operator-Based Linearization scheme, which allows us to perform large-scale simulations with full physics in a reasonable time. The following conclusions can be made:

- The capillary transition zone shortens the onset time of convection and enhances the dissolution rate caused by gravitational instabilities. These numerical results validate the great accuracy of our new thermodynamic model and linearization approach for predicting the short- and long-term CO_2 propagation.
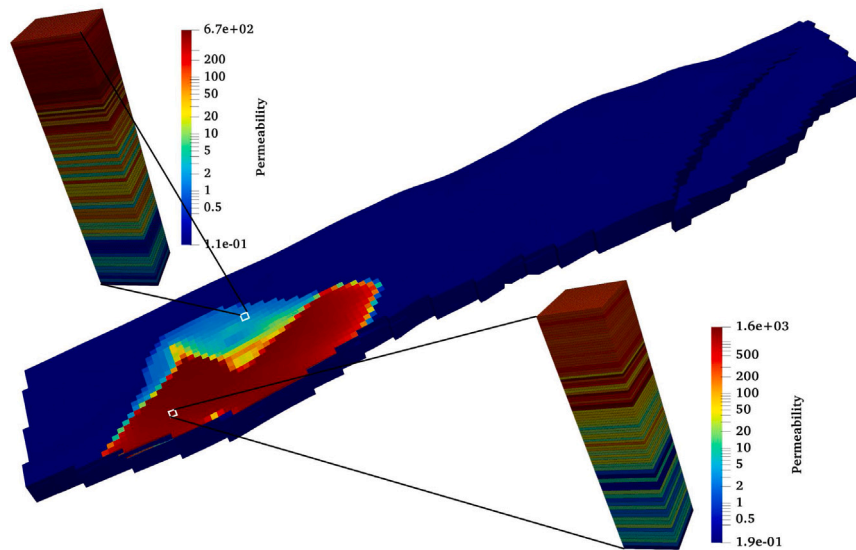
Fig. 14. Location of two representative elements.

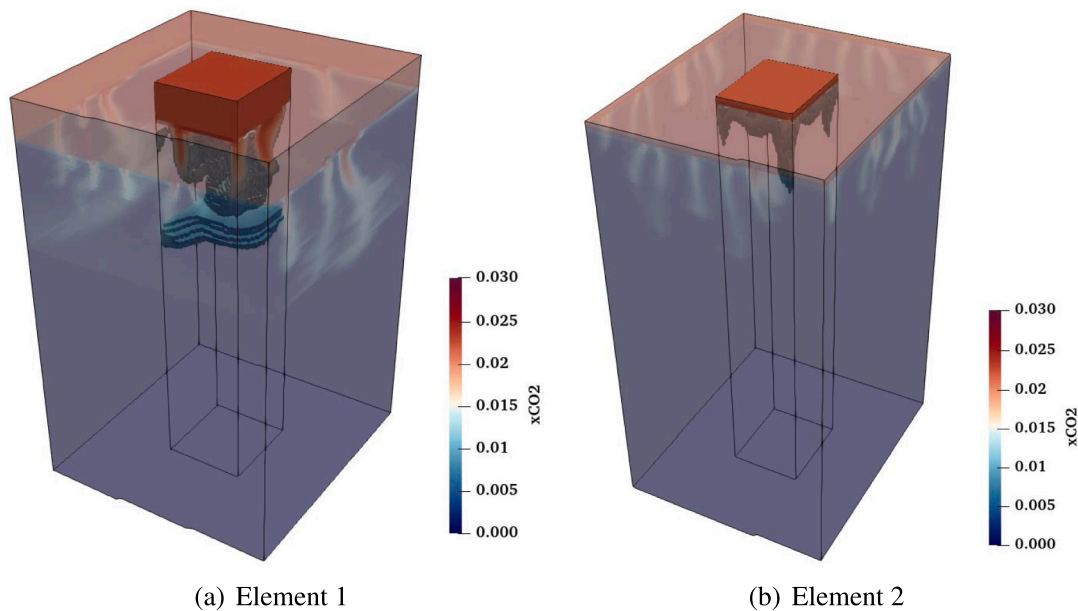(a) Element 1   (b) Element 2

Fig. 15. CO_2 mole fraction after 100 years in different elements, and a threshold ([0.008, 0.03]) is applied.

- With consideration of thermal conduction, a smooth temperature gradient is observed; while thermal fingers are generated along with mass fingers if heat conduction is neglected. Due to the different directions of thermal gradient and concentration gradient, the onset time is postponed when thermal effects are taken into account; but, at the same time, the mass flux is enhanced.

- CO_2 fingers can move outward in all directions in a 3D model, leading to larger and flatter fingers. It has a negligible effect on the onset of convection but increases the mass flux by approximately 20%.

- In the short-run, CO_2 exists mainly in porous media as free gas and residual gas, while the amount of dissolved gas is relatively small. Once the buoyancy-driven convection dominates the flow, dissolution trapping is the main mechanism for permanent trapping.

- There is a discrepancy in the mass transfer rate between the low- and high-resolution models. An advanced multi-scale technique is proposed for appropriate adjustment of the enhanced dissolution rate in the field-scale simulation of CO_2 sequestration.

CRediT authorship contribution statement

Xiaocong Lyu: Methodology, Writing the code, Data analysis, Writing – review & editing. **Denis Voskov:** Methodology, Supervision, Writing – review & editing.

Declaration of competing interest

The authors declare that they have no known competing financial interests or personal relationships that could have appeared to influence the work reported in this paper.

Data availability
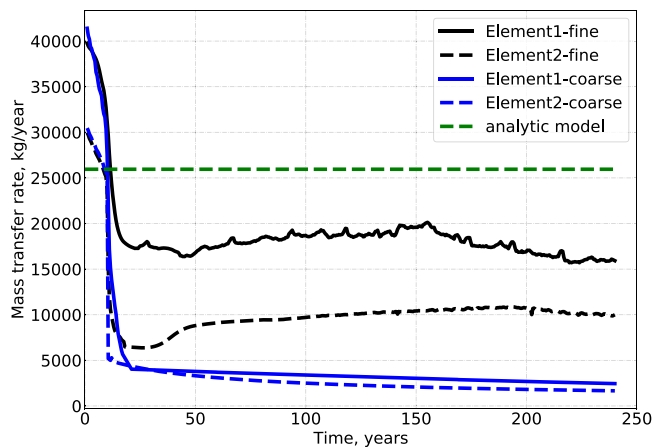
Data will be made available on request.

Fig. 16. Variations of Mass transfer rate of each element with different mesh resolution. 'fine' stands for the results obtained from new mesh, and 'coarse' is the results from the original mesh.

Acknowledgments

References

Anderson, J., Bachu, S., Nimir, H., Basu, B., Bradshaw, J., Deguchi, G., Gale, J., Von Goerne, G., Heidug, W., Holloway, S., 2005. Underground geological storage. Cambridge University Press, ISBN-13 978-0-521-86643-9.

Class, H., Ebigbo, A., Helmig, R., Dahle, H.K., Nordbotten, J.M., Celia, M.A., Audigane, P., Darcis, M., Ennis-King, J., Fan, Y., 2009. A benchmark study on problems related to CO2 storage in geologic formations. Comput. Geosci. 13 (4), 409–434. http://dx.doi.org/10.1007/s10596-009-9146-x.

Duan, Z., Sun, R., 2003. An improved model calculating CO2 solubility in pure water and aqueous NaCl solutions from 273 to 533 K and from 0 to 2000 bar. Chem. Geol. 193 (3–4), 257–271. http://dx.doi.org/10.1016/S0009-2541(02)00263-2.

Elenius, M.T., Nordbotten, J.M., Kalisch, H., 2012. Effects of a capillary transition zone on the stability of a diffusive boundary layer. IMA J. Appl. Math. 77 (6), 771–787. http://dx.doi.org/10.1093/imamat/hxs054.

Elenius, M.T., Nordbotten, J.M., Kalisch, H., 2014. Convective mixing influenced by the capillary transition zone. Comput. Geosci. 18 (3–4), 417–431. http://dx.doi.org/10.1007/s10596-014-9415-1.

Elenius, M., Voskov, D., Tchelepi, H., 2015. Interactions between gravity currents and convective dissolution. Adv. Water Resour. 83, 77–88. http://dx.doi.org/10.1016/j.advwatres.2015.05.006.

Ennis-King, J.P., Paterson, L., 2005. Role of convective mixing in the long-term storage of carbon dioxide in deep saline formations. SPE J. 10 (03), 349–356. http://dx.doi.org/10.2118/84344-PA.

Ennis-King, J., Preston, I., Paterson, L., 2005. Onset of convection in anisotropic porous media subject to a rapid change in boundary conditions. Phys. Fluids 17 (8), 084107. http://dx.doi.org/10.1063/1.2033911.

Ezekiel, J., Ebigbo, A., Adams, B.M., Saar, M.O., 2020. Combining natural gas recovery and CO2-based geothermal energy extraction for electric power generation. Appl. Energy 269, 115012. http://dx.doi.org/10.1016/j.apenergy.2020.115012.

Farajzadeh, R., Zitha, P.L., Bruining, J., 2009. Enhanced mass transfer of CO2 into water: experiment and modeling. Ind. Eng. Chem. Res. 48 (13), 6423–6431. http://dx.doi.org/10.1021/ie801521u.

Gasda, S.E., Nilsen, H.M., Dahle, H.K., Gray, W.G., 2012. Effective models for CO2 migration in geological systems with varying topography. Water Resour. Res. 48 (10), http://dx.doi.org/10.1029/2012WR012264.

Gilfillan, S.M., Lollar, B.S., Holland, G., Blagburn, D., Stevens, S., Schoell, M., Cassidy, M., Ding, Z., Zhou, Z., Lacrampe-Couloume, G., 2009. Solubility trapping in formation water as dominant CO2 sink in natural gas fields. Nature 458 (7238), 614–618. http://dx.doi.org/10.1038/nature07852.

Guo, Y., Li, J., Ahmed, R., Shen, N., Li, X., 2019. An enthalpy model of CO2-CH4-H2S-N2-brine systems applied in simulation of non-isothermal multiphase and multicomponent flow with high pressure, temperature and salinity. J. CO2 Util. 31, 85–97. http://dx.doi.org/10.1016/j.jcou.2019.02.018.

Iranshahr, A., Voskov, D.V., Tchelepi, H.A., 2013a. A negative-flash tie-simplex approach for multiphase reservoir simulation. SPE J. 18 (6), 1140–1149. http://dx.doi.org/10.2118/141896-PA.

Iranshahr, A., Voskov, D.V., Tchelepi, H.A., 2013b. Tie-simplex based compositional space parameterization: Continuity and generalization to multiphase systems. AIChE J. 59 (5), 1684–1701. http://dx.doi.org/10.1002/aic.13919.

Islam, A.W., Carlson, E.S., 2012. Viscosity models and effects of dissolved CO2. Energy Fuels 26 (8), 5330–5336. http://dx.doi.org/10.1021/EF3006228.

Jafari Raad, S.M., Hassanzadeh, H., Ennis-King, J., 2019. On the dynamics of two-component convective dissolution in porous media. Water Resour. Res. 55 (5), 4030–4042. http://dx.doi.org/10.1029/2018WR024572.

Khait, M., Voskov, D., 2018. Adaptive parameterization for solving of thermal/compositional nonlinear flow and transport with buoyancy. SPE J. 23, 522–534. http://dx.doi.org/10.2118/182685-PA.

Kong, X.-Z., Saar, M.O., 2013. Numerical study of the effects of permeability heterogeneity on density-driven convective mixing during CO2 dissolution storage. Int. J. Greenh. Gas Control 19, 160–173. http://dx.doi.org/10.1016/j.ijggc.2013.08.020.

Kritchevsky, I., Iliinskaya, A., 1945. Partial molal volumes of gases dissolved in liquids. (A contribution to the thermodynamics of dilute solutions of non-electrolytes). Acta Physicochim. URSS 20 (3), 327–348.

Li, B., Tchelepi, H.A., Benson, S.M., 2013. Influence of capillary-pressure models on CO2 solubility trapping. Adv. Water Resour. 62, 488–498. http://dx.doi.org/10.1016/j.advwatres.2013.08.005.

Li, D., Zhang, H., Li, Y., Xu, W., Jiang, X., 2018. Effects of N2 and H2S binary impurities on CO2 geological storage in stratified formation–a sensitivity study. Appl. Energy 229, 482–492. http://dx.doi.org/10.1016/j.apenergy.2018.07.083.

Lindeberg, E., Wessel-Berg, D., 1997. Vertical convection in an aquifer column under a gas cap of CO2. Energy Convers. Manage. 38, S229–S234. http://dx.doi.org/10.1016/S0196-8904(96)00274-9.

Linstrom, P.J., Mallard, W.G., 2001. The NIST chemistry WebBook: A chemical data resource on the internet. J. Chem. Eng. Data 46 (5), 1059–1063. http://dx.doi.org/10.1021/je000236i.

Lyu, X., Khait, M., Voskov, D., 2021a. Operator-based linearization approach for modeling of multiphase flow with buoyancy and capillarity. SPE J. (ISSN: 1086-055X) 26, http://dx.doi.org/10.2118/205378-PA.

Lyu, X., Voskov, D., R.Rossen, W., 2021b. Numerical investigations of foam-assisted CO2 storage in saline aquifers. Int. J. Greenh. Gas Control 108, 103314. http://dx.doi.org/10.1016/j.ijggc.2021.103314.

MacMinn, C., Szulczewski, M., Juanes, R., 2011. CO2 migration in saline aquifers. Part 2. Capillary and solubility trapping. J. Fluid Mech. 688, 321–351. http://dx.doi.org/10.1017/jfm.2011.379.

Mao, S., Duan, Z., 2009. The viscosity of aqueous alkali-chloride solutions up to 623 K, 1,000 bar, and high ionic strength. Int. J. Thermophys. 30 (5), 1510–1523. http://dx.doi.org/10.1007/s10765-009-0646-7.

Martinez, M.J., Hesse, M.A., 2016. Two-phase convective CO2 dissolution in saline aquifers. Water Resour. Res. 52 (1), 585–599. http://dx.doi.org/10.1002/2015WR017085.

Meng, Q., Jiang, X., 2014. Numerical analyses of the solubility trapping of CO2 storage in geological formations. Appl. Energy 130, 581–591. http://dx.doi.org/10.1016/j.apenergy.2014.01.037.

Neufeld, J.A., Hesse, M.A., Riaz, A., Hallworth, M.A., Tchelepi, H.A., Huppert, H.E., 2010. Convective dissolution of carbon dioxide in saline aquifers. Geophys. Res. Lett. 37 (22), http://dx.doi.org/10.1029/2010GL044728.

Pau, G.S., Bell, J.B., Pruess, K., Almgren, A.S., Lijewski, M.J., Zhang, K., 2010. High-resolution simulation and characterization of density-driven flow in CO2 storage in saline aquifers. Adv. Water Resour. 33 (4), 443–455. http://dx.doi.org/10.1016/j.advwatres.2010.01.009.

Pruess, K., Zhang, K., 2008. Numerical modeling studies of the dissolution-diffusion-convection process during CO2 storage in saline aquifers. Technical report, Lawrence Berkeley National Lab.(LBNL), Berkeley, CA (United States), http://dx.doi.org/10.2172/944124.

Riaz, A., Hesse, M., Tchelepi, H., Orr, F., 2006. Onset of convection in a gravitationally unstable diffusive boundary layer in porous media. J. Fluid Mech. 548, 87–111. http://dx.doi.org/10.1017/S0022112005007494.

Riaz, A., Tchelepi, H., 2007. Stability of two-phase vertical flow in homogeneous porous media. Phys. Fluids 19 (7), 072103. http://dx.doi.org/10.1063/1.2742975.

Schrag, D.P., 2007. Preparing to capture carbon. Science 315 (5813), 812–813. http://dx.doi.org/10.1126/science.1137632.

Slim, A.C., 2014. Solutal-convection regimes in a two-dimensional porous medium. J. Fluid Mech. 741, 461. http://dx.doi.org/10.1017/jfm.2013.673.

Slim, A.C., Bandi, M.M., Miller, J.C., Mahadevan, L., 2013. Dissolution-driven convection in a Hele–Shaw cell. Phys. Fluids 25 (2), 024101. http://dx.doi.org/10.1063/1.4790511.

Someva, S., Nishio, M., Chen, B., Okamoto, K., Uchida, T., 2000. The effect of pressure, temperature and salinity on CO2 dissolution into H2O+ nacl. In: Fluids Engineering Division 2000: Proceedings of the ASME Presented At the 2000 ASME International Mechanical Engineering Congress and Exposition, November 5-10, 2000, Orlando, Florida. American Society of Mechanical Engineers, pp. 197–203.

Spycher, N., Pruess, K., Ennis-King, J., 2003. CO2-H2O mixtures in the geological sequestration of CO2. i. assessment and calculation of mutual solubilities from 12 to 100 C and up to 600 bar. Geochim. Cosmochim. Acta 67 (16), 3015–3031. http://dx.doi.org/10.1016/j.gca.2005.01.015.

Szulczewski, M.L., MacMinn, C.W., Herzog, H.J., Juanes, R., 2012. Lifetime of carbon capture and storage as a climate-change mitigation technology. Proc. Natl. Acad. Sci. 109 (14), 5185–5189. http://dx.doi.org/10.1073/pnas.1115347109.

Taheri, A., Wessel-Berg, D., Torsaeter, O., Soroush, M., 2012. The effects of anisotropy and heterogeneity on CO2 dissolution in deep saline aquifers. In: Carbon Management Technology Conference. OnePetro, http://dx.doi.org/10.7122/151345-MS.

Voskov, D., 2017. Operator-based linearization approach for modeling of multiphase multi-component flow in porous media. J. Comput. Phys. 337, 275–288. http://dx.doi.org/10.1016/j.jcp.2017.02.041.

Voskov, D.V., Tchelepi, H.A., 2012. Comparison of nonlinear formulations for two-phase multi-component eos based simulation. J. Pet. Sci. Eng. 82, 101–111. http://dx.doi.org/10.1016/j.petrol.2011.10.012.

Wang, Y., Voskov, D., Khait, M., Bruhn, D., 2020. An efficient numerical simulator for geothermal simulation: A benchmark study. Appl. Energy 264, http://dx.doi.org/10.1016/j.apenergy.2020.114693.

Xu, X., Chen, S., Zhang, D., 2006. Convective stability analysis of the long-term storage of carbon dioxide in deep saline aquifers. Adv. Water Resour. 29 (3), 397–407. http://dx.doi.org/10.1016/j.advwatres.2005.05.008.